RSC Advances

PAPER

View Article Online
View Journal | View Issue

Cite this: *RSC Adv.*, 2026, **16**, 24675

From anti-solvent synthesis to polaron-driven transport: exploring the promise of lead-free Rb_2SnCl_6 nanocrystals

Abderraouf Jraba, *[a] Saber Nasri, [bc] Iheb Garoui,[b] Abderrazek Oueslati [b] and Elimame Elaloui[a]

Received 6th February 2026
Accepted 7th May 2026

DOI: 10.1039/d6ra01082b

rsc.li/rsc-advances

Lead-free double perovskites have emerged as promising alternatives to toxic lead-based halide perovskites. In this work, Rb_2SnCl_6 nanocrystals were synthesized *via* an anti-solvent precipitation route and systematically investigated to elucidate their structural, optical, and electrical properties. X-ray diffraction combined with Rietveld refinement confirms the formation of a single-phase cubic structure with space group $Fm\bar{3}m$, while transmission electron microscopy reveals well-defined prismatic nanocrystals with an average particle size of ~50 nm. X-ray photoelectron spectroscopy verifies the presence of Rb^+, Sn^{4+}, and Cl^- ions in their expected oxidation states, confirming the chemical purity and structural stability of the material. Optical characterization indicates a wide direct band gap of approximately 4.69 eV and strong ultraviolet absorption, highlighting the suitability of Rb_2SnCl_6 for UV optoelectronic applications. Broadband impedance spectroscopy conducted over a wide temperature and frequency range reveals thermally activated electrical transport with pronounced negative temperature coefficient of resistance behavior. Analysis of AC conductivity using Jonscher's power law and frequency exponent evolution identifies overlapping large polaron tunneling (OLPT) as the dominant charge transport mechanism. The low activation energy and stable dielectric response underscore the potential of Rb_2SnCl_6 as a robust lead-free material for UV-photodetectors, radiation sensors, solid-state electrolytes, and high-frequency electronic devices.

Introduction

The escalating global energy crisis, intensified by relentless industrial expansion and the looming threats of climate change, calls for transformative advances in renewable energy technologies.[1–3] Among the myriad solutions, UV optoelectronics, solid-state ionics, and radiation-sensing technologies emerge as critical pillars for a sustainable and technologically advanced future.[4] These technologies demand novel materials that transcend mere efficiency, requiring environmental compatibility, economic feasibility, and resilience against diverse operational stresses. Silicon-based solar cells, a long-standing industry standard, face inherent limitations including high manufacturing costs and rigid processing protocols, which curb their adaptability for widespread use. As a result, research efforts have increasingly gravitated towards exploring alternative semiconductors that can be synthesized through cost-effective methods while exhibiting superior optoelectronic performance.[5,6]

Metal halide perovskites have revolutionized this quest, especially lead-based three-dimensional perovskites that demonstrate exceptional light absorption, charge transport properties, and power conversion efficiencies exceeding 25% within less than a decade of development.[7] However, their practical deployment is significantly hampered by the toxicity of lead and their susceptibility to environmental degradation, particularly in the presence of moisture, oxygen, and heat.[8,9] This has galvanized the scientific community to innovate lead-free variants that retain the desirable optoelectronic qualities but offer enhanced stability and safety. Tin(IV)-based vacancy-ordered double perovskites of the form A_2SnCl_6, where A represents alkali metal ions such as cesium, rubidium, or potassium, have prominently surfaced in this context. Their unique structure consists of isolated $[SnCl_6]^{2-}$ octahedra, generating a robust three-dimensional lattice with vacant sites that facilitates rapid halide ion migration.[10] This architecture endows them with wide electrochemical windows, low electronic conductivity, and superior resistance to photochemical deterioration, making these materials highly promising for UV optoelectronic applications, including photodetectors, scintillators, and radiation sensors, as well as solid electrolytes in next-generation chloride-ion battery systems.[11–13]

---

[a] *Laboratory of the Application of Materials to Water, the Environment, and Energy LAM3E, Gafsa University, Faculty of Sciences of Gafsa, Department of Chemistry, Sidi Ahmed Zarroug, 2100 Gafsa, Tunisia. E-mail: jrabaraoof@gmail.com*

[b] *Laboratory of Spectroscopic Characterization and Optical Materials, Faculty of Sciences, University of Sfax, B. P. 1171, 3000 Sfax, Tunisia*

[c] *University of Gafsa, Preparatory Institute for Engineering Studies of Gafsa, El Khayzorane Street – Zaroug, Gafsa – 2112, Tunsia*

The role of the A-site alkali cation in these perovskites is critical, profoundly influencing lattice spacing, vibrational dynamics, ion migration pathways, and charge transport efficacy.[14,15] In particular, replacing the smaller potassium ion in K_2SnCl_6 with the larger rubidium ion in Rb_2SnCl_6 is theorized to expand the lattice, soften phonon modes, and drastically reduce the energy barriers for chloride ion hopping. Such structural transformations are expected to dramatically boost ionic conductivity and adjust the strength of polaron coupling, which in turn governs dielectric relaxation processes and overall electrical conduction. Moreover, the heavier and more polarizable Rb^+ cation can induce notable shifts in band structure and defect chemistry, opening avenues for tailored bandgap engineering and enhanced tolerance to defects, pivotal for stable optoelectronic device operation.[16,17] Despite these compelling theoretical advantages, detailed experimental investigations into Rb_2SnCl_6's dielectric behaviour, conduction mechanisms, relaxation dynamics, and polaron hopping phenomena are conspicuously scarce.[18,19]

The present study addresses this crucial knowledge gap by synthesizing phase-pure Rb_2SnCl_6 through a carefully optimized anti-solvent precipitation method. Comprehensive structural, morphological, and compositional characterization using X-ray diffraction with Rietveld refinement, scanning electron microscopy coupled with energy-dispersive X-ray spectroscopy, and X-ray photoelectron spectroscopy confirms material purity and crystallinity. Optical properties probed by UV-visible absorption provide insight into lattice vibrations and electronic transitions. Central to this work is an exhaustive examination of electrical properties through broadband impedance spectroscopy spanning wide temperature and frequency ranges. Using electric modulus formalism alongside AC and DC conductivity analyses, the study delves deeply into dielectric relaxation phenomena and elucidates ion transport mechanisms. The findings are further enriched through direct comparisons with K_2SnCl_6, revealing how incremental changes in A-site cation size and polarizability translate into significant modifications in activation energies, transport pathways, and the degree of polaronic conduction.[20,21]

Ultimately, this investigation substantiates Rb_2SnCl_6 as a highly promising lead-free, environmentally stable halide perovskite with versatile applications spanning solid-state electrolytes for energy storage to luminescent and photovoltaic devices. By illuminating its complex structure–property relationships and underlying conduction dynamics, the work not only fills critical experimental voids but also paves the way for informed, rational design of future halide double perovskites. These advances hold the potential to accelerate the transition to renewable, sustainable energy technologies while mitigating the environmental and health risks associated with lead-based materials.

Experimental section and methods

Synthesis procedure

Analytic rubidium chloride was reached from Merck (RbCl, reagent grade 99.95%), anhydrous tin chloride was reached from Merck ($SnCl_2$, reagent grade 99.98), analytical standard oleic acid was reached from Sigma Aldrich ($CH_3(CH_2)_7CH{=}CH(CH_2)_7COOH$, ≥98.5% GC grade), analytical acetonitrile was purchased from Merck (CH_3CN, analytical grade ≥98.0%), analytic toluene was reached from Merck ($C_6H_5CH_3$, ≥99.9% GC grade). All reagents were employed directly as purchased, without any additional purification steps.

The crystal powder was obtained through an anti-solvent precipitation method, building upon the synthesis strategy previously established.[47] The standard synthesis procedure involves dissolving 2 mmol of rubidium chloride (RbCl) and 1 mmol of tin(II) chloride ($SnCl_2$) in 12.5 mL of acetonitrile to obtain an atomic ratio Rb : Sn of 2 : 1. To stabilize the solution, 1.5 mL of oleic acid is added. The resulting mixture is stirred continuously at room temperature (28 °C) for 3 hours at a speed of 300 rpm under air atmosphere. Following this, the solution is introduced dropwise into 30 mL of toluene under constant stirring at 300 rpm. This step leads to the formation of a colloidal solid phase, turning the solution milky white. The reaction mixture is then transferred to a 100 mL ground-glass flask, and acetonitrile is removed *via* rotary evaporation at 85 °C under vacuum pumping. The resulting crystalline powder is separated from the toluene by centrifugation at 10 000 rpm for 5 minutes. The solid is subsequently washed three times with toluene and dried under infrared irradiation for 1 hour to yield the final Rb_2SnCl_6 product. This synthesis typically produces 300 ± 5 mg of Rb_2SnCl_6 powder, achieving an efficiency of 73% ± 2%. The synthesis procedure was repeated several times to obtain sufficient material for subsequent experiments.

Characterization techniques

The synthesized Rb_2SnCl_6 powder was thoroughly characterized using a combination of complementary techniques. Phase purity and crystal structure were confirmed by powder X-ray diffraction on a Philips X'Pert PRO diffractometer with Cu Kα radiation ($\lambda = 1.54187$ Å), collecting data from 10° to 70° (2θ) with a step of 0.013° and 3 s per step. Rietveld refinement was performed with FullProf Suite, and the refined structural model was visualized using Diamond software. Microstructural features and compositional analyses were carried out by high-resolution transmission electron microscopy on an FEI Tecnai G20 F20 instrument operated at 200 kV and equipped with an EDAX energy-dispersive X-ray detector. Surface chemical states were investigated by X-ray photoelectron spectroscopy on a Thermo Scientific K-Alpha+ spectrometer with monochromatic Al Kα radiation. High-resolution spectra of Rb 3d, Sn 3d, Cl 2p, C 1s, and O 1s regions were acquired at 50 eV pass energy, charge-referenced to adventitious carbon at 284.8 eV, and fitted using Thermo Avantage software after Shirley background subtraction. UV-vis absorption spectra were recorded using a Shimadzu UV-3101PC scanning spectrophotometer over the wavelength range of 200–1100 nm with a spectral resolution of 1 ± 0.2 nm. Baseline corrections were applied to eliminate instrumental drift. The acquired data provide a basis for determining the band gap energy after confirming the nature of the optical transition in Rb_2SnCl_6. Furthermore, these measurements allow for the determination of additional optical parameters, such as the Urbach energy and the extinction coefficient, providing insights into the dispersive behaviour of the compound. For electrical characterization, the powder was uniaxially pressed into dense pellets (8 mm diameter, ~1 mm thickness) under a 5-ton load and subsequently sintered at 100 ° C for 4 h. Platinum paste electrodes were applied to both polished pellet faces and cured at 80 °C for 1 h to ensure reliable electrical contact. Frequency-dependent impedance and dielectric measurements were performed using a Solartron 1260A impedance analyser over a frequency range of 10 Hz to 5 MHz with a 50 mV rms AC excitation, from 313 K to 423 K. All impedance spectra were fitted using equivalent-circuit models in ZView® software to deconvolute bulk, grain-boundary, and electrode contributions, enabling extraction of DC conductivity and dielectric relaxation parameters.

Results and discussion

Structure identification

The structure of Rb_2SnCl_6 perovskite nanocrystals was determined using FullProf Suite software, and the corresponding results are shown in Fig. 1. On the diffractogram, the red curve indicates experimental values, the black curve corresponds to the theoretical profile, while the purple curve represents the difference between the two. The short blue lines mark the positions where the theoretical diffraction peaks should appear, thus confirming that the synthesized nanocrystals adopt the known crystal structure of Rb_2SnCl_6 perovskite (CSD no. 2381630).

The detailed crystallographic parameters are reported in Table S1 (SI). The crystal structure of Rb_2SnCl_6 belongs to a cubic system, characterized by angles $\alpha = \beta = \gamma = 90°$ and a space group $Fm\bar{3}m$. The $SnCl_6^{2-}$ units form octahedra centred on Sn^{4+} ions with 2.417 Å of Sn–Cl bonds and 3.42 Å of edges, while the face-centred lattice was designed by Sn^{4+} cations with atomic position (0, 0, 0). The Rb^+ cations occupy the centres of the small cubes with edge length $a/2$ and surrounded by 4 $SnCl_6^{2-}$ octahedra's. The atomic position of Rb^+ is (0.25, 0.25, 0.25) while Cl^- occupies the (0.24, 0.00, 0.00) position (Table 1). The Rb_2SnCl_6 perovskite nanocrystals obtained in this work thus adopt the space group $Fm\bar{3}m$, with lattice parameters $a = b = c = 10.122$ Å, angles $\alpha = \beta = \gamma = 90°$, resulting a unit volume of 1037.1267 Å^3. Interatomic distances are $d_{Cl–Cl} = 3.42$ Å, $d_{Sn–Sn} = 7.15$ Å, $d_{Rb–Rb} = 5.06$ Å. Calculated atomic radius were 1.39 Å for Sn^{4+}, 2.2 Å for Rb^+, and 1.02 Å for Cl^-. The coordination of atoms was 6 for Sn, 12 for Rb, and 5 for Cl. The obtained refinement quality parameters reveal a good fit between the experimental diffractogram and the simulated profile. The low values of R_p (4.16) and R_{wp} (5.06) show that the model accurately reproduces the diffraction intensities measured across the entire 2θ angular range of the X-ray diagram, taking into account both the peak positions and their relative intensities. The R_{wp} factor, incorporating statistical weighting, is a more relevant indicator of the fit quality.

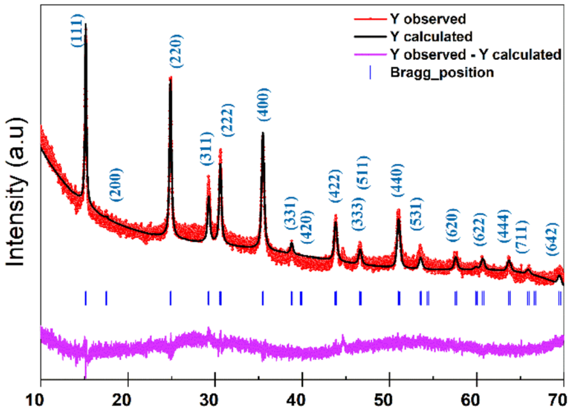

Fig. 1 X-ray diffraction (XRD) analysis of Rb_2SnCl_6 conducted at room temperature.

Table 1 Atomic positions, occupancy, and atoms multiplicity in Rb_2SnCl_6 double perovskite structure

	x	*y*	*z*	Biso	Occ	Mult
Sn	0.0000	0.0000	0.0000	0.66155	1	4
Cl	0.23886	0.0000	0.0000	0.51364	5.86	24
Rb	0.2500	0.2500	0.2500	0.79121	2.09	8

The value of R_{exp} (2.76) reflects satisfactory counting statistics and good experimental data quality. The quality factor $\chi^2 = 3.2686$ exceeds the ideal value of 1 but remains within an acceptable range, frequently observed for nanostructured systems. This difference can be explained by the presence of microstructural effects, such as the crystallite size distribution, lattice microstresses, or a slight preferential orientation.

Overall, the low R_p and R_{wp} values associated with a moderate χ^2 confirm the reliability of the refinement and indicate that the adopted structural model accurately accounts for the crystallographic properties of the fabricated Rb_2SnCl_6 nanocrystals.

The relative intensities of the diffraction peaks were analysed to assess possible preferred orientation in the powder sample. The relative intensity for each (*hkl*) plane was calculated using the expression:[22]

$$I_{R(hkl)} = \frac{I_{(hkl)}}{\sum I_{(hkl)}} \times 100 \tag{1}$$

where $I_{(hkl)}$ reveal the intensity of (*hkl*) plane, $\sum I_{(hkl)}$ reveal the sum of (*hkl*) peaks intensity and obtained results are presented in Table 2. The calculated results, listed in Table 3 and plotted in Fig. 2, indicate that the (111) and (220) planes exhibit the highest relative intensities, revealing preferred orientations along these directions. These findings are consistent with those reported by K. Oukacha *et al.*[23]

The X-ray diffraction patterns were thoroughly examined using the Williamson–Hall (W–H) approach.[24] This technique is based on an established empirical relation, termed the Williamson–Hall equation, that links the broadening of diffraction peaks-specifically the full width at half maximum (β)-to the

Table 2 *hkl*, D_{hkl}, and $I_{R(hkl)}$ parameters of prepared Rb_2SnCl_6 double perovskite calculated by FullProf suite software

h	*k*	*l*	Mult	$D_{(hkl)}$ (Å)	2*θ* (°)	FWHM	I_{hkl}	$I_{R(hkl)}$ (%)
1	1	1	8	5.8122	15.2445	0.1929	1931.14	29.6622
2	2	0	12	3.5664	24.968	0.1929	1681.34	25.82529
3	1	1	24	3.05028	29.2798	0.2755	411.15	6.315241
2	2	2	8	2.91408	30.6811	0.3031	815.54	12.52665
4	0	0	6	2.52416	35.5673	0.3306	1007.97	15.48236
4	2	2	24	2.06266	43.8952	0.2755	318.63	4.894139
4	4	0	12	1.78688	51.1183	0.3306	344.67	5.294112

Table 3 Atomic ratio quantification of present element in Rb_2SnCl_6 nanocrystals perovskite

Element	Weight%	Average%	Atomic%	Average%
Cl K1	42.40	43.40 ± 1.0	55.80	58.20 ± 2.40
Cl K2	44.40		60.60	
Sn L1	22.50	22.65 ± 0.15	19.70	18.90 ± 0.80
Sn L2	22.80		18.10	
Rb K1	35.10	33.95 ± 1.15	24.50	22.9 ± 1.60
Rb K2	32.80		21.30	

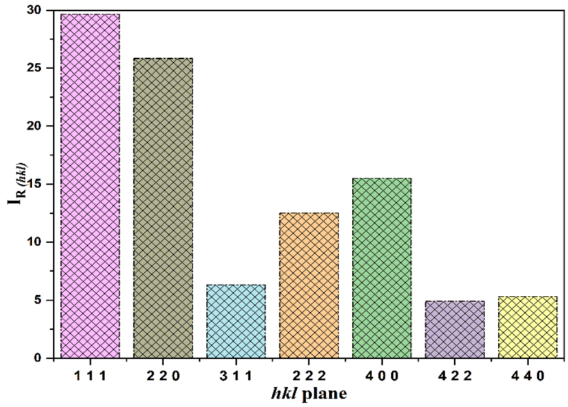

Fig. 2 Calculated data: $I_{R(hkl)}$ as function of (*hkl*) diffraction plane.

microstrain (ε) present in the crystal lattice. The corresponding equation is given by:

$$\beta \cos \theta = \frac{K\lambda}{D} + 4\varepsilon \sin \theta \qquad (2)$$

In the Williamson–Hall equation, the parameters are defined as follows: K is the shape factor (commonly taken as 0.89), λ is the X-ray wavelength (1.5406 Å for Cu-Kα radiation), D represents the average crystallite size, θ is the Bragg diffraction angle, β is the full width at half maximum (FWHM) of the diffraction peak, and ε denotes the lattice microstrain.

The Williamson–Hall plot (Fig. 3) displays $\beta\cos(\theta)$ plotted against $4\sin(\theta)$, with a linear regression fitted to the data points. In analogy to the standard linear form $y = mx + c$, the slope (m) of the fit corresponds to the lattice microstrain (ε), whereas the y-intercept (c) allows calculation of the average crystallite size (D). This analysis yields an average crystallite size of approximately 41.73 nm and a lattice microstrain of 0.018×10^{-3}.

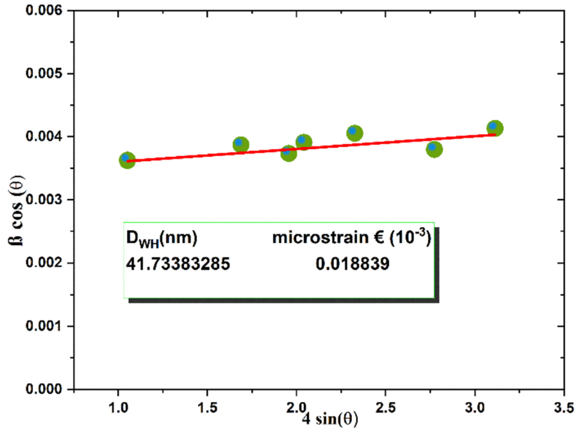

Fig. 3 Williamson–Hall analysis used to evaluate crystallite size and microstrain in Rb_2SnCl_6.

Microstructural features and analysis

TEM analysis showed that prepared Rb_2SnCl_6 nanoperovskites presented a prismatic shape (Fig. 4a). The obtained result is in coincidence with those reported previously which confirm the conventional shape of crystalline structure.[25,26] The average particles size calculated by ImageJ software presented in Fig. 4b show that prepared crystals are in nanometric scale with an average particles size of 50 nm. The EDX analyses shown in Fig. 4c and d were performed at two distinct points (1 and 2) indicated in Fig. 4a. The resulting spectra exhibit characteristic peaks at approximately 1.8, 13.4, and 14.9 eV, corresponding to the Rb signals. Peaks observed in the region between 3 and 4 eV confirm the presence of Sn. The detection of Cl is evidenced by the peaks located at 2.6 and 2.8 eV. Overall, the EDX spectra confirm the high purity of the synthesized product, with no detectable chemical contamination.

Quantitative elemental analysis (Table 3) reveals atomic compositions of 22.9% ± 1.60 for rubidium, 18.90% ± 0.80 for tin, and 58.20% ± 2.40 for chlorine. The resulting Cl/Sn ratio of approximately 3.1 is therefore considered a lower bound. The phase stoichiometry is more reliably established by Rietveld refinement of the XRD data, which confirms Cl occupancy of 5.86 out of 6 (theoretical). This result can be explained by the fact that EDX is a semi-quantitative technique, and the quantification of light halogen elements such as Cl is subject to systematic underestimation due to matrix absorption effects and detection efficiency variations. The slight discrepancy between the particle size measured by TEM (~50 nm) and the crystallite size estimated from the Williamson–Hall (W–H) method (~41 nm) is typical for nanomaterials. This difference arises because TEM visualizes secondary particles or agglomerates, whereas the W–H analysis from XRD provides the size of coherent diffracting domains within primary crystallites. The approximately 20% smaller W–H value reflects mild lattice microstrain or defects that contribute to diffraction peak broadening, which is common in polycrystalline nanoparticles composed of multiple crystallites aggregated into larger observable particles.[27] Such nanoscale coherence confirms the material's suitability for applications requiring uniform short-range charge transport, like solid electrolytes.

X-ray photoelectron spectroscopy (XPS) analysis

XPS analysis was performed to determine the surface chemical composition and oxidation states of the constituent elements of Rb_2SnCl_6 perovskite nanocrystals. Measurements were carried out using an Al Kα X-ray gun emitted by an aluminium source, providing stable monochromatic excitation suitable for analysing the binding energies of the studied elements. The survey XPS spectrum of the nanocrystals is shown in Fig. 5 and demonstrates the presence of Rb, Sn, and Cl, consistent with the expected composition of Rb_2SnCl_6.

To ensure optimal accuracy, all spectra were calibrated using the C 1s peak of the C–C bond, located at 284.80 eV (Fig. 6a), as a reference, thus correcting for any surface charge shifts.[28] All binding energies of different elements are reported in Table 4, ΔE reveal the standard energy differences between peaks used for spectrum deconvolution.

Detailed analysis of the high-resolution regions reveals the characteristic electronic signatures of each element. Fig. 6b shows the decomposition of the 3d doublet of rubidium, the $3d_{5/2}$ and $3d_{3/2}$ peaks are clearly observed at 110.08 eV and 111.38 eV, respectively. The observed spin–orbit separation is consistent with values reported in the literature, confirming the presence of Rb^+ in the crystal architecture.[29] Fig. 6c shows the $3d_{5/2}$ and $3d_{3/2}$ peaks of tin, located at 487.08 eV and 495.48 eV. These bond energy values correspond to the +4-oxidation state of tin, characteristic of Rb_2SnCl_2 type perovskites.[30] No additional lower-energy peaks were detected, indicating the absence of Sn^{2+} or metallic tin impurities, thus confirming the chemical purity of the nanocrystals. Fig. 6d shows the XPS region of chlorine, the characteristic $2p_{3/2}$ and $2p_{1/2}$ peaks appear at 198.58 eV and 200.18 eV, respectively, with the expected spin–orbit separation for Cl^- in a halogenated structure.[31] The intensity and position of these peaks indicate a stable chemical bond between chlorine and tetravalent tin.

All these results are consistent with data previously reported in the literature for Rb_2SnCl_6 materials. They confirm not only

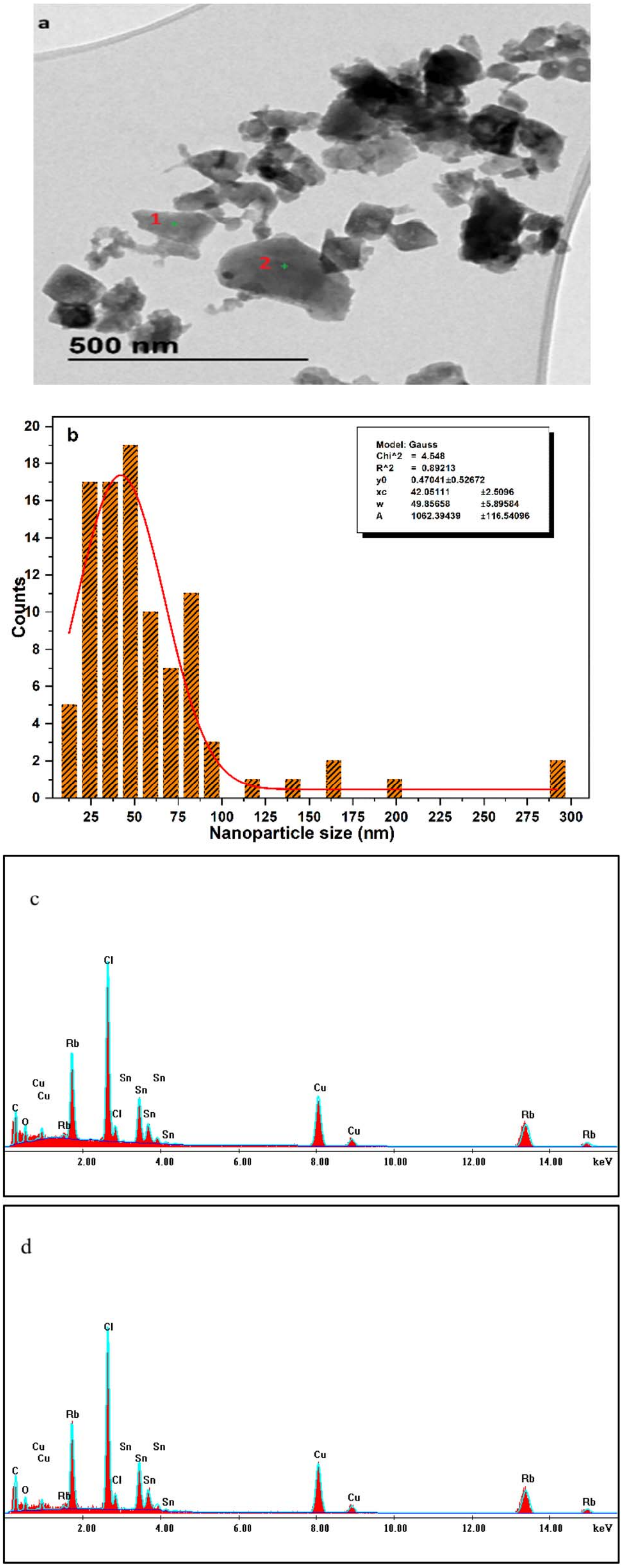

Fig. 4 TEM-EDX of prepared Rb_2SnCl_6: 500 nm TEM photo of perovskite structure (a), nanoparticle size distribution calculated by ImageJ software (b), elemental EDX spectrum measured in first point (c), and elemental EDX spectrum measured in second point (d).

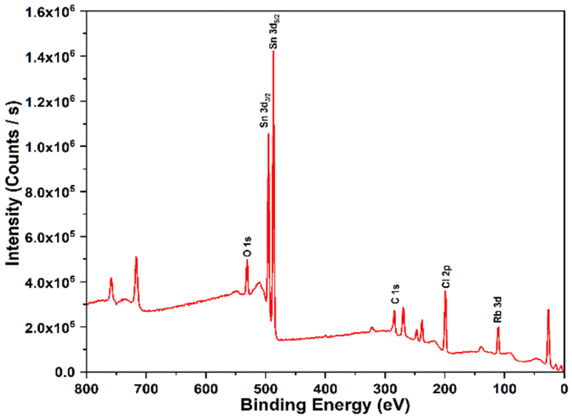

Fig. 5 XPS survey of prepared Rb_2SnCl_6 double perovskite nanocrystal using an Al Kα X-ray gun and 150.0 eV pass energy with step of 1 eV.

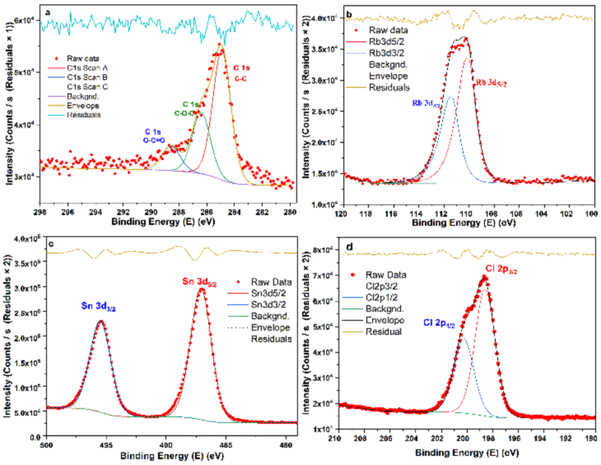

Fig. 6 Detailed XPS analysis of the high-resolution regions of different present elements: carbon analysis C 1s (a), rubidium analysis Rb 3d (b), tin analysis Sn 3d (c), and chlorine analysis Cl 2p (d).

Table 4 Binding energy of Rb 3d, Sn 3d, Cl 2p and C 1s among Rb_2SnCl_6 double perovskite nanocrystal[a]

Binding energy (eV)						
Rb 3d		Sn 3d		Cl 2p		C 1s
$3d_{3/2}$	$3d_{5/2}$	$3d_{3/2}$	$3d_{5/2}$	$2p_{1/2}$	$2p_{3/2}$	1s
111.38	110.08	495.48	487.08	200.18	198.58	284.80
$\Delta E = 1.3$		$\Delta E = 8.4$		$\Delta E = 1.6$		ND

[a] ND: energy difference is not defined for singular peak of 1s spin orbit.

the presence of the constituent elements in the correct oxidation states (Rb^+, Sn^{4+}, Cl^-), but also the crystallochemical quality and stability of the synthesized perovskite structure proved in XRD analysis. These findings are consistent with previously reported XPS data for Rb_2SnCl_6 and related materials, verifying the presence of Rb^+, Sn^{4+}, and Cl^- in their anticipated oxidation states. It is important to emphasize that XPS is a surface analysis technique, limited to the first few nanometres of the material; thus, the determined oxidation states essentially reflect the surface chemistry. However, the consistency with the EDX and XRD results, as well as the absence of secondary phases, indicates that the core structure and overall stoichiometry of the prepared Rb_2SnCl_6 nanocrystals remain intact.

Optical and electronic characterization using UV-vis spectroscopy

The investigation of optical properties in vacancy-ordered double-perovskite halides, such as Rb_2SnCl_6, is of significant interest for emerging applications in UV photodetection, scintillation detectors, radiation sensing, and phosphor host matrices for dopant-activated luminescence. UV-visible spectroscopy provides an effective tool for characterizing absorption behaviour and deriving key optical constants, offering valuable insights into the semiconductor band structure and defect-related states. Absorbance measurements, in particular, elucidate photon–material interactions, including band-to-band transitions and sub-bandgap absorption processes. Consequently, these optical studies are crucial for determining fundamental parameters such as the bandgap energy (E_g), the Urbach energy (associated with tail states and disorder), and the electron–phonon interaction strength. The optical absorption behaviour of the synthesized Rb_2SnCl_6 vacancy-ordered double perovskite was investigated using UV-visible diffuse reflectance spectroscopy. The absorbance spectrum as a function of wavelength is presented in Fig. 7. The material exhibits strong absorption in the ultraviolet region below ~300 nm, followed by a sharp absorption edge extending into the near-visible range, with relatively low absorbance in the visible region (>400 nm). This profile is characteristic of wide-bandgap halide perovskites, where the intense UV absorption arises primarily from charge-transfer transitions involving the $[SnCl_6]^{2-}$ octahedral units. The inset in Fig. 7 shows the first derivative of absorbance with respect to wavelength (or energy), revealing a clear inflection point that marks the onset of the fundamental absorption edge, providing an initial estimate of the optical bandgap. The band gap is identified at the peak of this plot, as shown in the inset of Fig. 7, yielding a value of $E_g = 4.69$ eV. The estimated band gap energies of Rb_2SnCl_6 fall within the typical semiconductor range (0.5–5 eV), classifying it specifically as a wide band gap semiconductor.[32]

To identify both the nature and magnitude of the optical band gap, Tauc analyses were performed considering allowed indirect and direct electronic transitions.[33] The representation of $(\alpha h\nu)^2$ as a function of photon energy exhibits a clear linear regime, and extrapolation of this region to the energy axis provides a direct band gap value of about 4.69 eV (Fig. 8), which is very close to the experimentally observed absorption edge. Conversely, the plot of $(\alpha h\nu)^{1/2}$ *versus* $h\nu$ shows weak linearity and a less reliable extrapolation, indicating that an indirect transition is unlikely. The close agreement between the direct Tauc band gap and the observed optical threshold confirms that Rb_2SnCl_6 is a direct band gap material. This behaviour is in line

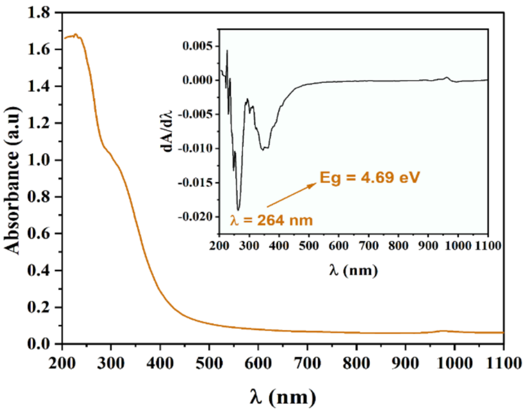

Fig. 7 Variation of the absorbance *versus* wavelength for Rb_2SnCl_6. The derivative of absorbance in the inset.

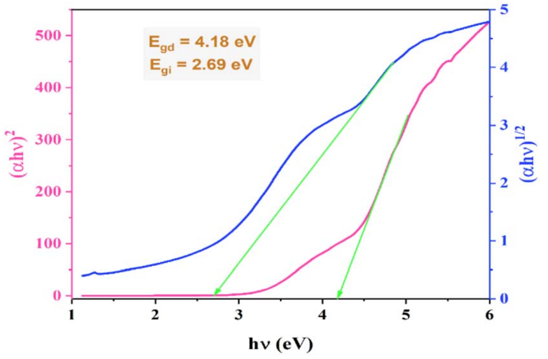

Fig. 8 Variation of $(\alpha h\nu)^{1/2}$ and $(\alpha h\nu)^2$ *versus* $(h\nu)$.

with previous theoretical and experimental studies on A_2SnX_6 vacancy-ordered double perovskites, where both the valence band maximum and conduction band minimum are located at the same *k*-point in the Brillouin zone, supporting their suitability for optoelectronic applications that rely on efficient radiative recombination.[34]

Sub-bandgap absorption behaviour was examined using the Urbach tail analysis (Fig. 9). The plot of ln(α) *versus* photon energy in the exponential absorption region below the band edge exhibits a linear dependence, from which the Urbach energy (E_u) was extracted.

The obtained E_u value of approximately 0.5 eV is consistent with values reported for polycrystalline A_2SnCl_6 nanopowder samples, reflecting the combined contributions of grain boundary disorder, intrinsic structural vacancies in the $[SnCl_6]^{2-}$ sublattice, surface ligand states, and phonon broadening.[35] While this value is higher than those reported for high-quality single crystals, it is typical for solution-processed polycrystalline nanoparticles and should be interpreted in that context. A contribution from local Cl-site disorder cannot be excluded and is consistent with the semi-quantitative EDX data.

For optoelectronic applications, the threshold wavelength (λ_T) serves as a crucial indicator of performance. It marks the longest wavelength of incoming radiation that the material can absorb, thereby defining the spectral window in which it can operate effectively. By identifying this limit, one can assess the material's suitability for devices such as solar cells, photodetectors, and other light-harvesting technologies. The threshold wavelength λ_T was determined using the following expression:[36]

$$\left(\frac{\alpha}{\lambda}\right)^2 = C\left(\frac{1}{\lambda}\right) - \left(\frac{1}{\lambda_T}\right) \tag{3}$$

In this equation, "α" denotes the absorption coefficient, "λ" corresponds to the wavelength of the incoming light, and "C" is a constant that depends on the material. From the fitting of the experimental data using eqn (3), the threshold wavelength (λ_T) of the Rb_2SnCl_6 compound was found to be 298 nm, as shown in Fig. 10. This result confirms that the material exhibits strong absorption in the UV region.

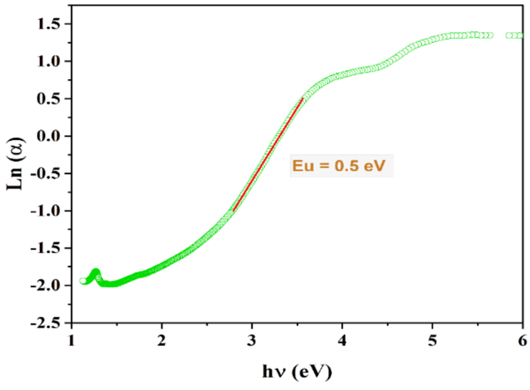

Fig. 9 ln(α) *versus* ($h\nu$) to determine the Urbach energy E_u, for the Rb_2SnCl_6 compound.

Overall, the optical characterization establishes Rb_2SnCl_6 as a wide direct bandgap semiconductor (~4.69 eV), characterized by strong ultraviolet absorption and a sharp absorption edge. The negligible absorption in the visible region is consistent with its colourless appearance and underscores its suitability for applications that require high visible transparency alongside efficient UV responsiveness, such as UV photodetectors, scintillators, and host matrices for dopant-activated luminescence. In conjunction with these favourable optical features, the lead-free nature and all-inorganic composition of Rb_2SnCl_6 further enhance its technological appeal, positioning it as a robust lead-free material for UV photodetectors, radiation sensors, scintillators, and solid-state electrolytes.[37]

Electrical properties investigated by impedance spectroscopy

Electrochemical impedance spectroscopy (EIS) is a versatile and powerful experimental approach widely employed to investigate the electrical response and charge-transport characteristics of semiconductor and electrochemical materials. In this technique, the response of Rb_2SnCl_6 to a small-amplitude alternating electric field is monitored over a broad frequency domain, allowing the analysis of energy storage and dissipation mechanisms governed by the material's intrinsic electrical properties.[38] EIS is particularly effective for probing charge carrier dynamics and for separating the contributions arising from electrode effects, bulk (grain) conduction, and grain boundary relaxation processes, as extensively documented in previous studies.[39] The overall impedance response is described by a complex quantity, consisting of a real component

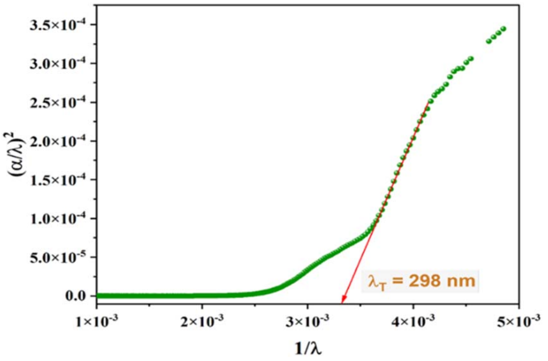

Fig. 10 $(\alpha/\lambda)^2$ *vs.* $1/\lambda$ plots for the Rb_2SnCl_6 compound.

associated with resistive behaviour and an imaginary component related to capacitive effects, expressed as:

$$Z^* = Z' + jZ'' \tag{4}$$

Fig. 11 shows the variation of the real part of complex impedance (Z') with angular frequency for Rb_2SnCl_6 across 303–393 K. The plots reveal distinct low- and high-frequency regimes: low frequencies display a frequency-independent plateau, characteristic of DC conduction *via* long-range hopping between $[SnCl_6]^{2-}$ units, while high frequencies exhibit pronounced dispersion from localized carrier motion and incomplete hops.

This separation underscores dual conduction pathways—bulk DC transport at low frequencies *versus* space-charge limited AC processes at high frequencies. The transition frequency shifts rightward with temperature, indicating thermally activated barrier lowering and enhanced mobility.

At high frequencies, Z' plateaus to a temperature-independent minimum, reflecting polarization saturation. Low-frequency Z' decreases markedly with rising temperature, exhibiting negative temperature coefficient of resistance (NTCR) behaviour typical of wide-bandgap semiconductors, confirming Rb_2SnCl_6's thermistor potential linked to its direct gap and low Urbach tails.[40]

The imaginary part of the impedance ($-Z''$) offers critical insights into the dielectric relaxation processes in Rb_2SnCl_6, which arise from the motion of charge carriers and/or the re-orientation of dipolar species in response to the applied alternating electric field. As depicted in Fig. 12, the variation of $-Z''$ with angular frequency is presented over a temperature range of 303–393 K. Each spectrum displays a well-defined relaxation peak, positioned in the frequency region corresponding to the transition from DC to AC conduction regimes, as previously observed in the real part of the impedance (Z', Fig. 11).

This peak corresponds to the relaxation frequency, marking the crossover from long-range charge carrier migration (at lower frequencies) to short-range, localized hopping or reorientation (at higher frequencies). The asymmetric broadening of these peaks with increasing temperature signifies a deviation from ideal Debye-type relaxation, indicative of a distribution of relaxation times and complex polarization mechanisms inherent to polycrystalline halide perovskites.[41]

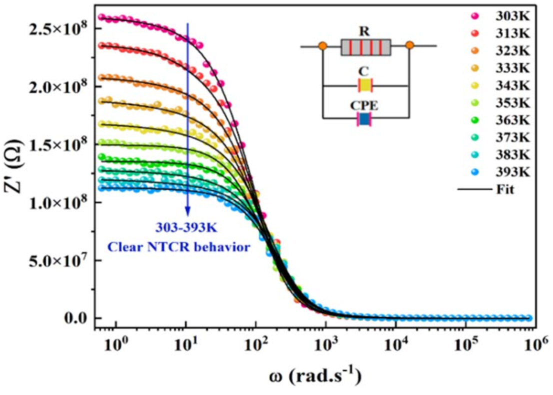

Fig. 11 Evolution of the real part of impedance (Z') as a function of angular frequency at various temperatures for Rb_2SnCl_6.

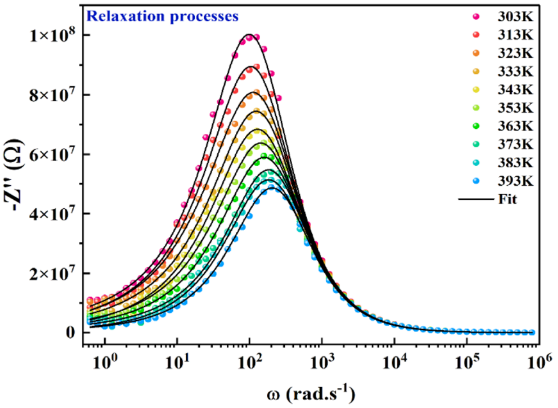

Fig. 12 Evolution of the imaginary part of impedance (Z'') as a function of angular frequency at various temperatures for Rb_2SnCl_6.

To model the impedance data accurately, fitting was performed using ZView software, which identified the most appropriate equivalent circuit (inset of Fig. 11) consisting of a parallel combination of a resistor (R), a constant phase element (CPE), and a capacitor (C).[42] The corresponding fitting parameters are summarized in Table 5.

The data compiled in Table 6 shows a pronounced decrease in electrical resistivity with increasing temperature, confirming the semiconducting nature of the sample. To determine characteristic parameters such as the activation energy, sensitivity constant, and stability factor, the dependence of ln(RT) on the inverse temperature (1000/T) is presented in Fig. 13. The plot displays a well-defined linear relationship, demonstrating that the resistivity diminishes systematically as temperature increases, which is characteristic of materials exhibiting a negative temperature coefficient of resistance (NTCR).

Over the examined temperature interval, the experimental results are well described by the Arrhenius-type relation:

$$R = \frac{A}{T}\exp\left(\frac{E_a}{k_B T}\right) \tag{5}$$

where A is the pre-exponential constant, k_B denotes Boltzmann's constant, and E_a corresponds to the activation energy. The

Table 5 Electrical values of the equivalent circuit parameters calculated for Rb_2SnCl_6 compound at different temperatures

T (K)	R (10^8 Ω)	C (10^{-11} F)	Q (10^{-11} F)	α
303	2.595	3.306	7.339	0.66768
313	2.345	3.324	10.90	0.62625
323	2.124	3.314	11.99	0.62980
333	1.888	3.302	11.86	0.64161
343	1.648	3.305	8.592	0.66833
353	1.509	3.243	8.515	0.70323
363	1.380	3.270	9.863	0.68329
373	1.264	3.253	7.112	0.72031
383	1.192	3.283	8.585	0.69663
393	1.139	3.256	7.288	0.72516

Table 6 Summary of frequency-evolved parameters within the overlapping large polaron tunnelling framework

	Frequency (kHz)	W_{H0} (eV)	N (eV^{-1} cm^{-1})	α ($Å^{-1}$)	r_p (Å)	R_ω (Å)
OLPT model	39.81	0.11	4.25×10^{35}	0.32	1.31	2.97
	10	0.13	7.61×10^{34}	0.30	1.20	2.89
	2.51	0.15	1.70×10^{34}	0.29	1.11	2.71
	0.39	0.17	4.20×10^{33}	0.28	0.98	2.68

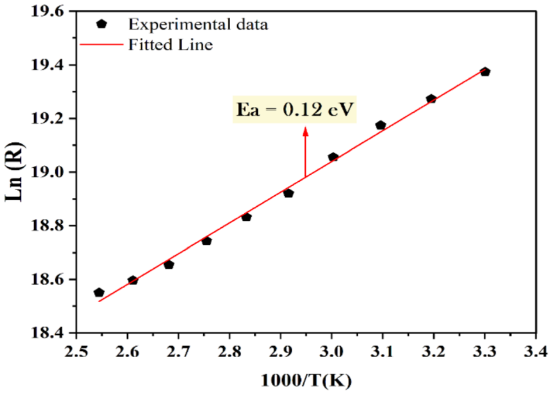

Fig. 13 Evolution of ln(R) against (1000/T).

strong linearity observed in Fig. 13, supported by a high correlation coefficient ($R^2 = 0.99587$), confirms that charge transport is governed by a thermally activated conduction mechanism. From the slope of the fitted line, the activation energy was estimated to be approximately 0.12 eV. The low activation energy of 0.12 eV and pronounced NTCR behaviour align with the insulating character of vacancy-ordered double perovskites like Rb_2SnCl_6, where isolated $[SnCl_6]^{2-}$ octahedra limit free carrier generation, but thermal excitation enables modest charge hopping.

Electrical conductivity

In light of the experimentally determined optical band gap, the investigated compound can be categorized as a semiconductor, displaying an increase in electrical conductivity with rising temperature. This trend is characteristic of thermally activated charge transport, where charge carriers acquire sufficient energy to participate in conduction. In particular, thermally activated charge transport is governed by both carrier concentration and mobility; increasing temperature enhances these factors by enabling a larger number of carriers to overcome energy barriers and migrate through the lattice, thereby improving overall conductivity.[43] Temperature-dependent conduction behaviour is of considerable importance for a wide range of technological applications, including electronic components and photovoltaic systems.[44] To further elucidate the electrical transport mechanisms and to determine the parameters controlling conduction in Rb_2SnCl_6, the frequency dependence of electrical conductivity was investigated at different temperatures as illustrated in Fig. 14.

In the low-frequency region, the conductivity attains a plateau corresponding to the DC component, which is essentially frequency-independent. At higher frequencies, the conductivity exhibits a marked dispersion arising from the AC contribution. In this regime, charge carriers undergo thermally activated hopping, resulting in random diffusion at low frequencies that yields the DC conductivity σ_{dc}. Meanwhile, in the dispersive region, charge carriers oscillate back and forth in a correlated fashion. According to the jump-relaxation framework developed by Funke and Hoppe, the coexistence of a frequency-independent DC plateau and a frequency-dependent AC part is explained by the balance between successful and unsuccessful hops: at low frequencies, successful long-range hops dominate the transport, whereas at high frequencies the proportion of unsuccessful hops increases, leading to the pronounced dispersion observed in the conductivity spectra.[45]

The AC conductivity spectrum is described by the empirical Jonscher power law:[46]

$$\sigma_{ac} = \sigma_{dc} + A\omega^s \tag{6}$$

Here, σ_{dc} denotes the material's DC conductivity, A is the pre-exponential factor, ω is the angular frequency, and s is the power-law exponent. Fig. 15 presents the temperature dependence of the dc conductivity in the form of a plot of ln($\sigma_{dc}T$) *versus* 1000/T, which follows an Arrhenius-type behaviour commonly employed to describe charge transport in ceramic

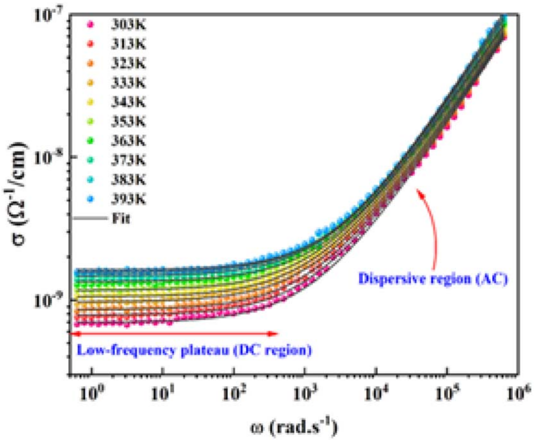

Fig. 14 Electrical conductivity spectra of the studied system at various temperatures.

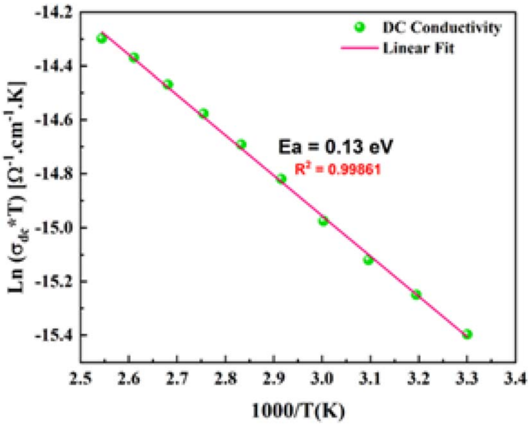

Fig. 15 Variation of $\ln(\sigma_{dc}T)$ *versus* $(1000/T)$ of the Rb_2SnCl_6 compound.

materials. The dc conductivity can be expressed using the Arrhenius relation:

$$\sigma_{dc} = T\sigma_0 \exp(k_B T - E_a) \quad (7)$$

where σ_0 denotes the pre-exponential conductivity factor, k_B is Boltzmann's constant, and E_a corresponds to the activation energy for charge transport. From the linear fit of the experimental data, the activation energy was extracted and found to be $E_a = 0.13$ eV.

To elucidate the dominant charge-transport mechanism in the investigated material, several theoretical frameworks describing the temperature dependence of the ac conductivity, $\sigma(T)$, were examined. In disordered systems, the evolution of the frequency exponent $s(T)$ with temperature is widely recognized as a reliable indicator of the underlying conduction process. Various models have been proposed to interpret this behaviour.[47]

The quantum mechanical tunnelling (QMT) model assumes that charge carriers are transferred between localized states by tunnelling through potential barriers without the need for thermal activation; as a result, the exponent s remains almost insensitive to temperature. In contrast, the correlated barrier hopping (CBH) model attributes electrical transport to thermally activated hopping of carriers between defect states separated by energy barriers, leading to a gradual reduction of s with increasing temperature.[48]

The non-overlapping small polaron tunnelling (NSPT) model considers charge transport *via* thermally assisted tunnelling of small polarons between isolated sites, which is manifested by an increase in the exponent s as temperature rises. Alternatively, the overlapping large polaron tunneling (OLPT) model describes conduction through tunneling of large polarons across overlapping potential wells; in this case, $s(T)$ increases at lower temperatures, reaches a maximum, and subsequently decreases at elevated temperatures.[49,50]

A comparison between the experimentally obtained $s(T)$ behaviour and these theoretical predictions allow the identification of the most probable conduction mechanism governing charge transport in the studied compound. Fig. 16 depicts the temperature dependence of the frequency exponent s, showing an initial decrease followed by a modest rise at elevated temperatures. Such a non-monotonic evolution of s is characteristic of the overlapping large polaron tunnelling (OLPT) mechanism, indicating that charge transport is governed by the motion of large polarons through overlapping potential landscapes. Within the OLPT framework, ac conductivity originates from the tunnelling of polarons influenced by interactions between their associated lattice distortion fields.[51] In the case of large polarons, strong Coulomb interactions extend the spatial reach of the potential wells, allowing neighbouring wells to overlap or partially merge. This overlap substantially lowers the effective energy barrier for polaron transfer between adjacent sites, thereby promoting charge carrier mobility and enhancing the ac conductivity. The reduced hopping barrier minimizes the energy required for carrier motion and directly affects the associated dielectric losses. Consequently, the overlap of potential wells, driven by long-range Coulomb interactions, plays a pivotal role in enabling efficient polaron tunnelling across the lattice.

In the case of Rb_2SnCl_6, the isolated $[SnCl_6]^{2-}$ octahedra serve as primary polaron centres, where Sn^{4+}–Cl^- covalent bonding generates lattice distortions upon charge localization. The Rb^+ cations, being highly polarizable and mobile within the vacancy-ordered $Fm\bar{3}m$ framework, facilitate polaron formation through dynamic lattice relaxation. The interaction between these polarons and the surrounding chloride lattice creates expansive distortion fields that drive the tunnelling process characteristic of OLPT.

The merging of potential wells arises from long-range Coulomb interactions between neighbouring $[SnCl_6]^{2-}$ units, substantially lowering the hopping barrier compared to small polaron models. This reduction stems from Rb_2SnCl_6's specific structural features: the high polarizability of Sn^{4+} (d^{10} configuration) enhances well overlap, while rigid octahedral isolation enforces anisotropic tunnelling paths. The vacancy-ordered structure provides a stable scaffold, supporting efficient polaron motion without phase instability.

This polaron dynamics governs Rb_2SnCl_6's electrical response, particularly in wide-bandgap semiconductors where

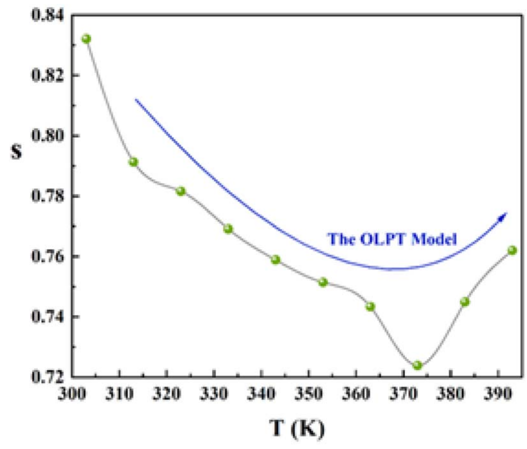

Fig. 16 The temperature dependence of the frequency exponent "s".

band conduction is suppressed. In UV optoelectronics and radiation sensors, where charge transport relies on polaron hopping, tailoring polaron size *via* Cl substitution or doping can optimize both electronic mobility and dielectric response. The OLPT mechanism proves especially relevant in Rb_2SnCl_6 due to its lead-free all-inorganic environment.

The temperature/frequency dependence of AC conductivity further validates this: elevated temperatures supply activation energy to expand polaron radii and deepen well overlap, boosting σ_{ac}; higher frequencies enable rapid polaron reorientation within the alternating field. These traits position Rb_2SnCl_6 as a promising material for high-frequency capacitors, UV photodetectors, and radiation-hardened thermistors, where polaron tunnelling delivers low-loss operation across a broad frequency range, benefiting from the inherent structural advantages of the all-inorganic vacancy-ordered framework.

Within the framework of the OLPT model, the ac conductivity is described by the relation:

$$\sigma_{ac} = \frac{\pi^4 e^2 {k_B}^2 T^2 \alpha^{-1} \omega \left(N(E_F)^2\right) {R_\omega}^4}{12\left(2\alpha k_B T + \frac{W_{H0} r_p}{{R_\omega}^2}\right)} \tag{8}$$

The value of the jump distance R_ω is obtained by solving the equation below

$$R_\omega'^2 + [\omega_{H0} + \ln(\omega\tau_0)]R_\omega' - \omega_{H0} r_0' = 0 \tag{9}$$

Within this relation, $R_\omega' = 2\alpha R_\omega,\ r_0' = 2\alpha r_0,\ \beta = \frac{1}{k_B T}$, in this context, α corresponds to the reciprocal of the localization length.

Within the framework of the overlapping large polaron tunnelling (OLPT) model, the potential wells of large polarons at adjacent sites merge, resulting in a decreased energy requirement for polaron transfer, as described in the following.[52]

$$W_H = W_{H0}\left[1 - \frac{r_p}{R}\right] \tag{10}$$

In this framework, W_{H0} represents the energy required for polaron hopping, R denotes the distance between polaron sites, and r_p corresponds to the polaron size. It is further assumed that W_{H0} remains constant across all sites, while the site separation R is treated as a variable. The values of W_{H0} and R_ω can be determined using the expressions provided below:[53]

$$W_{H0} = \frac{e^2}{4\varepsilon_p r_p} \tag{11}$$

$$R_\omega = \frac{1}{4\alpha}\left\{\left(\ln\left(\frac{1}{\tau_0}\right) - W_{H0}\beta\right) + \left[\left(W_{H0}\beta - \ln\left(\frac{1}{\tau_0}\right)\right)^2 + 8\alpha W_{H0} r_p \beta\right]^{\frac{1}{2}}\right\} \tag{12}$$

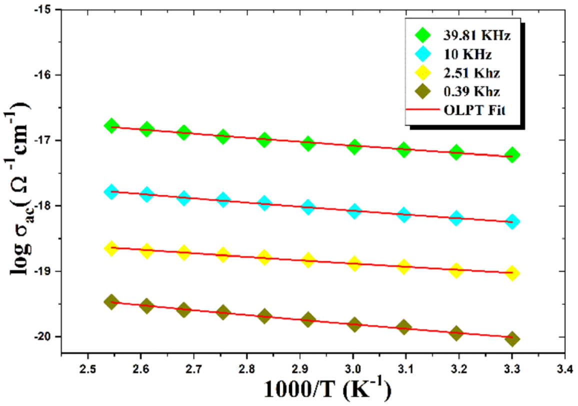

Fig. 17 Temperature evolution of AC conductivity plotted against 1000/*T*, analysed using the OLPT mechanism.

The frequency factor "*s*" in this setup is described as:

$$s = 1 - \frac{8\alpha R_\omega + \frac{6W_{H0} r_p}{R_\omega k_B T}}{\left(2\alpha R_\omega + \left(\frac{W_{H0} r_p}{R_\omega k_B T}\right)\right)^2} \tag{13}$$

As depicted in Fig. 17, the OLPT model closely reproduces the observed experimental behaviour. The fitting parameters utilized in this analysis are listed in Table 6.

Conclusions

In this study, phase-pure Rb_2SnCl_6 vacancy-ordered double perovskite nanocrystals were successfully synthesized using a facile anti-solvent precipitation method and comprehensively characterized to establish their structural, optical, and electrical properties. Structural analyses confirmed a highly crystalline cubic $Fm\bar{3}m$ phase with nanoscale coherence, while microscopic and compositional investigations validated the uniform morphology and stoichiometric integrity of the synthesized material. XPS measurements further confirmed the stable oxidation states of Rb^+, Sn^{4+}, and Cl^-, demonstrating the chemical robustness of the perovskite framework.

Optical studies revealed that Rb_2SnCl_6 is a wide direct bandgap semiconductor (≈4.69 eV) with strong ultraviolet absorption and minimal visible-light absorption, making it particularly attractive for UV optoelectronic and radiation-detection applications. Electrical characterization *via* impedance spectroscopy demonstrated thermally activated conduction with clear negative temperature coefficient of resistance behaviour. Detailed analysis of AC conductivity and frequency-dependent transport parameters established overlapping large polaron tunnelling as the dominant charge transport mechanism, enabled by the polarizable Rb^+ sublattice and the isolated $[SnCl_6]^{2-}$ octahedral units.

The combination of wide bandgap, low activation energy, stable dielectric response, and environmentally benign composition positions Rb_2SnCl_6 as a promising lead-free material for next-generation UV photodetectors, thermistors, solid-state electrolytes, and radiation-hardened electronic components. This work provides critical experimental insight into the structure–property–transport relationships of A_2SnCl_6 perovskites and offers a solid foundation for future efforts aimed at compositional tuning, defect engineering, and device-level integration. Finally, systematic long-term stability testing under controlled humidity, thermal cycling, and photo-oxidation conditions represents an important direction for future work.

Author contributions

Abderraouf Jraba: conceptualization, investigation, funding acquisition, writing – original draft, writing – review & editing, visualization, validation, methodology, software, formal analysis, data curation. Saber Nasri: conceptualization, investigation, funding acquisition, visualization, validation, methodology, data curation, software, formal analysis, writing – review & editing, writing – original draft. Iheb Garaoui: conceptualization, investigation, writing – original draft, funding acquisition, visualization, writing – review & editing, formal analysis, data curation. Abderrazek Oueslati: resources, supervision, data curation, project administration, visualization, writing – review & editing, funding acquisition, methodology, conceptualization, software, formal analysis. Elimame Elaloui: validation, project administration, resources, supervision, visualization, conceptualization, methodology, funding acquisition.

Conflicts of interest

The authors declare no conflict of interests in this work.

Data availability

The datasets generated and/or analysed during the current study are available from the corresponding authors upon reasonable request.

Supplementary information (SI) is available. See DOI: https://doi.org/10.1039/d6ra01082b.

Acknowledgements

The authors gratefully acknowledge the support provided by the Tunisian Ministry of Higher Education and Scientific Research.

Notes and references

1 I. Romdhane, A. Ajmi, M. Ben Bechir, *et al.*, Cs_2ZnCl_4: A Lead-Free All-Inorganic Perovskite with a Large Dielectric Permittivity, *RSC Adv.*, 2024, **14**, 36253, DOI: 10.1039/D4RA04755A.

2 X. Huang, Y. Wang, Y. Weng, Z. Yang and S. Dong, Stability, electronic, and optical properties of lead-free halide double perovskites $(CH_3NH_3)_2InBiX_6$ (X = halogen), *Phys. Rev. Mater.*, 2020, 104601, DOI: 10.1103/PhysRevMaterials.4.104601.

3 M. Younas, M. A. Gondal, M. A. Dastageer and U. Baig, Fabrication of cost-effective and efficient dye-sensitized solar cells with WO_3-TiO_2 nanocomposites as photoanode and MWCNT as Pt-free counter electrode, *Ceram. Int.*, 2019, 936–947, DOI: 10.1016/j.ceramint.2018.09.269.

4 A. G. Thate, K. S. Pakhare, S. S. Patil, *et al.*, Fabrication of TiO_2-ZnO nanocomposite photoanodes to enhance the dye-sensitized solar cell efficiency, *Res. Chem. Intermed.*, 2023, **49**, 147–168, DOI: 10.1007/s11164-022-04878-4.

5 F. Deschler, M. Price, S. Pathak, *et al.*, High Photoluminescence Efficiency and Optically Pumped Lasing in Solution-Processed Mixed Halide Perovskite Semiconductors, *J. Phys. Chem. Lett.*, 2014, **5**(8), 1421–1426, DOI: 10.1021/jz5005285.

6 Z. K. Tan, R. Moghaddam, M. Lai, *et al.*, Bright light-emitting diodes based on organometal halide perovskite, *Nat. Nanotechnol.*, 2014, **9**, 687–692, DOI: 10.1038/nnano.2014.149.

7 L. Doudou, X. Xulan, P. Jingyu and J. Wenyu, Perovskite light-emitting diodes with solution-processed MoO_3 films as the hole-transport layers, *J. Lumin.*, 2023, **256**, 119621, DOI: 10.1016/j.jlumin.2022.119621.

8 M. Ben Bechir and F. Alresheedib, Morphological, structural, optical and dielectric analysis of Cs_2TiBr_6 perovskite nanoparticles, *RSC Adv.*, 2024, **14**, 1634, DOI: 10.1039/D3RA06860A.

9 M. G. Brik and I. V. Kityk, Modeling of lattice constant and their relations with ionic radii and electronegativity of constituting ions of A2XY6 cubic crystals (A=K, Cs, Rb, Tl; X=tetravalent cation, Y=F, Cl, Br, I), *J. Phys. Chem. Solids*, 2011, **72**(11), 1256–1260, DOI: 10.1016/j.jpcs.2011.07.016.

10 H. Rahidul, Z. A. Hafiz, J. Rutva, A. L. Roger and A. Georgiy, Hydrothermal growth and characterization of large Rb2SnBr6 double perovskite crystals: a promising semiconductor material for photocatalysis and optoelectronics, *Dalton Trans.*, 2025, **54**, 3796, DOI: 10.1039/D4DT02712D.

11 M. Lyu, J. H. Yun and P. Chen, Addressing Toxicity of Lead: Progress and Applications of Low-Toxic Metal Halide Perovskites and Their Derivatives, *Adv. Energy Mater.*, 2017, **7**(15), 1602512, DOI: 10.1002/aenm.201602512.

12 M. H. Futscher and J. V. Milic, Mixed Conductivity of Hybrid Halide Perovskites: Emerging Opportunities and Challenges, *Front. Energy Res.*, 2021, **16**, 629074, DOI: 10.3389/fenrg.2021.629074.

13 A. Q. Sarmad, L. Tsai-Wei, T. Yi-Ting and L. Chun Che, Lead-free Rb_2SnCl_6:Bi Perovskite Nanocrystals for Luminescence Emission, *ACS Appl. Nano Mater.*, 2022, **5**(5), 7580–7587, DOI: 10.1021/acsanm.2c01647.

14 X. Chengyue, Z. Wenjun, L. Zhongfa, C. Zihan and D. Zhongyu, Temperature-controlled tunable emission of Bi^{3+}-doped Rb_2SnCl_6 all-inorganic vacancy ordered lead-free perovskite for advanced anticounterfeiting, *Dalton Trans.*, 2024, **53**(9), 4243–4250, DOI: 10.1039/D3DT04137A.

15 M. M. Lee, J. Teuscher, T. Miyasaka, T. N. Murakami and H. J. Snaith, Efficient hybrid solar cells based on meso-superstructured organometal halide perovskites, *Science*, 2012, **338**(6107), 643–647, DOI: 10.1126/science.1228604.

16 H. Qing, T. Huidong, W. Hezhen, P. Sihui, X. Yanqiao, J. Weihui, W. Lianjun and J. Wan, Facile preparation of highly efficient Te^{4+}-doped Rb_2SnCl_6 perovskites for white light-emitting diodes, *J. Lumin.*, 2023, **261**, 119904, DOI: 10.1016/j.jlumin.2023.119904.

17 A. A. Abeer, A. R. Syed, I. A.-M. Tahani, A. I. Aljameel, S. Bouzgarrou, H. H. Hegazy, A. Thamraa, N. Ghazanfar, M. Abeer and Q. Mahmood, New lead-free double perovskites $(Rb_2GeCl/Br)_6$; a promising materials for renewable energy applications, *Mater. Chem. Phys.*, 2021, **271**, 124876, DOI: 10.1016/j.matchemphys.2021.124876.

18 O. Alsalmia and M. Rashid, Study of structural, mechanical, thermal, and electronic structure properties of A_2SnCl_6 (A = Cs, Rb) perovskites for energy generation applications, *J. Ovonic Res.*, 2024, **20**(4), 537–549, DOI: 10.15251/JOR.2024.204.537.

19 K. Oukacha, L. Laânab and M. A. Bossi, Investigation of Microstructural and Optical Properties of Sol–Gel Halide-Substituted Rb_2SnCl_6 Double Perovskite, *J. Inorg. Organomet. Polym.*, 2025, **35**, 9679–9692, DOI: 10.1007/s10904-025-03871-9.

20 S. Kartik, T. Shigeyuki, I. Tamio, K. Kazuaki, S. Ryuhei, C. d. S. Egon, L. Hao, M. Rana and O. Shin-ichi, Unlocking the secrets of ideal fast ion conductors for all-solid-state batteries, *Commun. Mater.*, 2024, **5**(122), 1–27, DOI: 10.1038/s43246-024-00550-z.

21 L. Xiaona, T. K. Jung, L. Jing, Z. Changtai, X. Yang, M. Tao, L. Ruying, L. Jianwen and S. Xueliang, Structural regulation of halide superionic conductors for all-solid-state lithium batteries, *Nat. Commun.*, 2024, **15**(53), 1–8, DOI: 10.1038/s41467-023-43886-9.

22 R. Bekkari, L. laanab, D. Boyer, R. Mahiou and B. Jaber, Influence of the sol gel synthesis parameters on the photoluminescence properties of ZnO nanoparticles, *Mater. Sci. Semicond. Process.*, 2017, **71**(15), 181–187, DOI: 10.1016/j.mssp.2017.07.027.

23 K. Oukacha, L. Laanab, M. A. Bossi, S. E. Hajjaji and B. Jaber, Investigation of Microstructural and Optical Properties of Sol–Gel Halide-Substituted Rb_2SnCl_6 Double Perovskite, *J. Inorg. Organomet. Polym. Mater.*, 2025, **35**, 9679–9692, DOI: 10.1007/s10904-025-03871-9.

24 H. Chouhan, S. Prasad, B. N. Parida and R. K. Parida, Enhanced transport, dielectric and magnetic properties of Ni-doped $(YFeO_3)_{0.5}(BaTiO_3)_{0.5}$ perovskite for NTC thermistor and multifunctional applications, *Mater. Adv.*, 2025, **6**(14), 4778–4794, DOI: 10.1039/d4ma01233j.

25 A. K. Thomas, K. Abraham, J. Thomas and K. V. Saban, Electrical and dielectric behaviour of $Na_{0.5}La_{0.25}Sm_{0.25}Cu_3Ti_4O_{12}$ ceramics investigated by impedance and modulus spectroscopy, *J. Asian Ceram. Soc.*, 2017, **5**(1), 56–61, DOI: 10.1016/j.jascer.2017.01.002.

26 S. A. Qamar, T. W. Lin, Y. T. Tsai and C. C. Lin, Lead-free Rb_2SnCl_6:Bi Perovskite Nanocrystals for Luminescence Emission, *ACS Appl. Nano Mater.*, 2022, **5**(5), 7580–7587, DOI: 10.1021/acsanm.2c01647.

27 S. Ben Yahya, I. Garoui, M. Zaghrioui, A. Oueslati and B. Louati, Solid-state synthesized Li_4GeO_4 germanate: an exploration of its structure, vibrational characteristics, electrical conductivity, and dielectric properties, *RSC Adv.*, 2025, **15**(12), 9295–9304, DOI: 10.1039/d5ra01165e.

28 A. P. James, R. Jarrett, A. Hayat, A. Chris and V. S. Ranjani, Characterization of Carbon Products Produced by Catalytic Pyrolysis of Methane, *Microsc. Microanal.*, 2025, **31**(1), ozaf048.228, DOI: 10.1093/mam/ozaf048.228.

29 R. Ganesan, S. P. Vinodhini, R. Arulmozhi, *et al.*, Influence of halogen substitution in double perovskite $Rb_2Sn(Br_{0.75}I_{0.25})_6$ on the photocatalytic degradation of methylene blue dye under visible light irradiation, *J. Mater. Sci.: Mater. Electron.*, 2023, **34**(151), 1–16, DOI: 10.1007/s10854-022-09533-7.

30 R. Ganesan, S. P. Vinodhini, V. Balasubramani, G. Parthipan, T. M. Sridhar, R. Arulmozhi and R. Muralidharan, Tuning the band gap of hybrid lead free defect perovskite nano crystals for solar cell applications, *New J. Chem.*, 2019, **43**(38), 15258–15266, DOI: 10.1039/C9NJ03902C.

31 A. N. Nasrin, A. Al Mojahid and A. R. Mohammad, Band gap and optical property modulation under pressure in vacancy-ordered double perovskite Cs_2SeCl_6, *Comput. Theor. Chem.*, 2024, **1235**, 114572, DOI: 10.1016/j.comptc.2024.114572.

32 A. R. Zanatta, Revisiting the optical bandgap of semiconductors and the proposal of a unified methodology to its determination, *Sci. Rep.*, 2019, **9**, 11225, DOI: 10.1038/s41598-019-47670-.

33 M. Ben Gzaiel, I. Garoui, F. N. Almutairi, I. Mbarek and A. Oueslati, Lead-Free halide perovskites for optoelectronic application: Investigation of structural, optical, electric and dielectric behaviors, *Opt. Mater.*, 2024, **154**, 115664, DOI: 10.1016/j.optmat.2024.115664.

34 G. Shunfa, W. Ruirui, H. Qiuju, K. Degui and W. Wenzhi, Lead-free perovskite $Rb_2Sn_{1-x}Te_xCl_6$ with bright luminescence for optical thermometry and tunable white light emitting diodes, *J. Mater. Chem. C*, 2022, **10**(36), 13217–13224, DOI: 10.1039/D2TC02252D.

35 A. S. Aljaloud, A. Jebnouni, A. A. AlDheirib, *et al.*, Multifunctional Ionic and Dielectric Properties of Lead-Free Cs_2SnCl_6 Double Perovskite for Advanced Electronic Applications, *J. Electron. Mater.*, 2025, **54**, 11142–11154, DOI: 10.1007/s11664-025-12431-3.

36 A. B. J. Kharrat, K. Kahouli and S. Chaabouni, Detailed investigation of the optical properties of the $(C_8H_{11}BrN)_3BiCl_6$ compound by UV–visible measurements, *Bull. Mater. Sci.*, 2020, **43**(275), 1–9, DOI: 10.1007/s12034-020-02248-7.

37 K. Andreas, A. Maria, G. K. Athanassios, C. S. Constantinos, P. Dorothea, S. Eirini, R. Vasilios, T. Kalliopi, P. Vassilis, G. K. Mercouri and F. Polycarpos, Optical-Vibrational Properties of the Cs_2SnX_6 (X = Cl, Br, I) Defect Perovskites and Hole-Transport Efficiency in Dye-Sensitized Solar

Cells, *J. Phys. Chem. C*, 2016, **120**(22), 11777–11785, DOI: 10.1021/acs.jpcc.6b02175.

38 I. Garoui, S. Hajlaoui, I. Kammoun, A. Ouasri, J. Lhoste, H. Abid and A. Oueslati, Synthesis, crystal structure, BFDH morphology, Hirshfeld surface analysis and electrical characterization of the new bi-(2-amino-5-methylpyridinium) hexa-chlorostannate compound, *Phys. E*, 2024, **158**, 115897, DOI: 10.1016/j.physe.2024.115897.

39 I. Garoui, M. Mallek, F. N. Almutairi, W. Rekik and A. Oueslati, Synthesis, Structural characterization and complex impedance analysis of a novel organic-inorganic hybrid compound based on Mercury (II) chloride, *J. Mol. Struct.*, 2024, **1315**, 138881, DOI: 10.1016/j.molstruc.2024.138881.

40 M. Faizan, K. C. Bhamu, G. Murtaza, *et al.*, Electronic and optical properties of vacancy ordered double perovskites A_2BX_6 (A = Rb, Cs; B = Sn, Pd, Pt; and X = Cl, Br, I): a first principles study, *Sci. Rep.*, 2021, **11**, 6965, DOI: 10.1038/s41598-021-86145-x.

41 A. F. Mohamed, H. Rachid, C. Iskandar and G. Mohamed, Synthesis, crystal structure and electrical properties of the new organic-inorganic hybrid compound bis(1-chlorido-4-aminopyridinium) octachlorodiantimoinate, *Phys. E*, 2017, **94**, 167–173, DOI: 10.1016/j.physe.2017.08.010.

42 D. Johnson, *ZPlot, ZView Electrochemical Impedance Software, Version 2.3b*, Scribner Associates Inc., North Carolina, 2000.

43 Y. Lin, Q. Deng, Z. Ju, B. Cao and X. Zhang, Modelling and analysis of temperature dependence of electrical conductivity considering the effect of electron leaps, *Comput. Mater. Sci.*, 2025, **254**, 113910, DOI: 10.1016/j.commatsci.2025.113910.

44 M. Krimi, M. Akermi, R. Hassani and R. A. Ben, Optical and conduction mechanism study of lead-free $CsMnCl_3$ perovskite, *Solid State Sci.*, 2024, **155**, 107646, DOI: 10.1016/j.solidstatesciences.2024.107646.

45 K. Funke and R. Hoppe, Jump-relaxation model yields Kohlrausch-Williams-Watts behaviour, *Solid State Ionics*, 1990, **40**, 200–204, DOI: 10.1016/0167-2738(90)90321-H.

46 A. Lukichev, Nonlinear relaxation functions. Physical meaning of the Jonscher's power law, *J. Non-Cryst. Solids*, 2016, **442**, 17–21, DOI: 10.1016/j.jnoncrysol.2016.02.027.

47 S. Nasri, M. Megdiche and M. Gargouri, The investigation of dielectric properties and ac conductivity of new ceramic diphosphate $Ag_{0.6}Na_{0.4}FeP_2O_7$ using impedance spectroscopy method, *Phys. E*, 2016, **84**, 182–190, DOI: 10.1016/j.physe.2016.06.009.

48 S. Nasri, M. Megdiche and M. Gargouri, DC conductivity and study of AC electrical conduction mechanisms by non-overlapping small polaron tunneling model in $LiFeP_2O_7$ ceramic, *Ceram. Int.*, 2016, **42**, 943–951, DOI: 10.1016/j.ceramint.2015.09.023.

49 S. Nasri, A. Jraba, I. Garoui, A. Oueslati and E. Elaloui, Potassium tin chloride (K_2SnCl_6) as a lead-free perovskite: anti-solvent synthesis, structural characterization, and charge transport properties, *RSC Adv.*, 2025, **15**, 5369, DOI: 10.1039/D5RA00090D.

50 Z. Sami and M. Ben Bechir, Investigation of optical, dielectric, and charge transfer properties in lead-free double perovskite Cs_2MSbBr_6 (M = Cu, Ag), *Ionics*, 2024, **30**, 1177–1195, DOI: 10.1007/s11581-023-05300-8.

51 S. Nasri and A. Oueslatia, Exploring Li_2MgZrO_4 as a multifunctional material: structural analysis, polaron conductivity, and wide bandgap for energy and optoelectronic devices, *RSC Adv.*, 2025, **15**, 15516, DOI: 10.1039/d5ra02178b.

52 B. Bechir M and A. B. Rhaiem, Structural Phase Transition, Vibrational Analysis, Ionic Conductivity and Conduction Mechanism Studies in an Organic-Inorganic Hybrid Crystal: $[N(CH_3)_3H]_2CdCl_4$, *J. Solid State Chem.*, 2021, **296**, 122021, DOI: 10.1016/j.jssc.2021.122021.

53 F. Abdel-Wahab, M. Abdel-Baki and H. Abdel Maksoud, Insight into OLPT model conduction mechanism and dielectric relaxation of lead borate glass containing Cr and Ge ions, *Indian J. Phys.*, 2023, **97**, 1759–1768, DOI: 10.1007/s12648-022-02529-3.